Supplementary Information: Competing zero-field Chern insulators in Superconducting Twisted Bilayer Graphene

Petr Stepanov[1*], Ming Xie[2], Takashi Taniguchi[3], Kenji Watanabe[3], Xiaobo Lu[1], Allan H. MacDonald[2], B. Andrei Bernevig[4] and Dmitri K. Efetov[1*]

1. ICFO - Institut de Ciencies Fotoniques, The Barcelona Institute of Science and Technology, Castelldefels, Barcelona, 08860, Spain
2. Department of Physics, University of Texas at Austin, Austin, TX 78712, USA
3. National Institute of Material Sciences, 1-1 Namiki, Tsukuba, 305-0044, Japan
4. Department of Physics, Princeton University, Princeton, New Jersey 08544, USA

[*]Correspondence to: petr.stepanov@icfo.eu, dmitri.efetov@icfo.eu

A. Check for alignment to hBN.

To ensure that there is no alignment of crystallographic edges between graphene and either encapsulating hBN, we study a relative twist angle mismatch between the layers under optical microscope (Extended Data Fig. 1). White dashed line in the Extended Data Fig. 1a shows a naturally broken graphene edge that we ascribe to either zig-zag or armchair type. Similarly, orange and blue dashed lines in the Extended Data Fig. 1b and c, respectively, show naturally broken edges of the top and bottom hBN layers. White, orange and blue dashed lines in Extended Data Fig. 1d correspond to ones shown in the Extended Data Fig. 1a-c, and the numbers indicate relative twist angles between the naturally broken graphene edge and those found in hBN layers.

Extended Data Fig. 2 demonstrates Arrhenius plots for the superlattice unit cell fillings ν=0,±2, ±4. CNP at ν=0 shows a very weak dependence upon the decreasing T, which suggests no thermally activated gap. This is in a stark contrast with the hBN-aligned devices, which usually show large CNP gaps Δ_0≈6-7 meV due to sublattice symmetry breaking. CI states at ν=±2 show strong insulator-like thermal activation behavior with Δ_{-2}=1.49 meV, Δ_{+2}=1.67 meV. We also extract band insulator gaps Δ_{-4}=32 meV, Δ_{+4}=45 meV. We note that the band structure exhibits strong particle-hole asymmetry with the stronger band insulator on the conduction flat band side.

Lastly, Extended Data Fig. 3 demonstrates an extended range phase diagrams R_{xx} as a function of n and T beyond the flat band region. We note, that we do not observe additional satellite resistance peaks due to the interplay between the hBN/graphene moiré superlattice and the magnetic length that could be possibly assigned to alignment to hBN substrate. We note that in case of perfect (0°) alignment between hBN and graphene we expect to observe additional resistance peaks around n = 2.4×10^{12} cm^{-2}, which are completely absent in our measurements both inside and outside the flat band region.

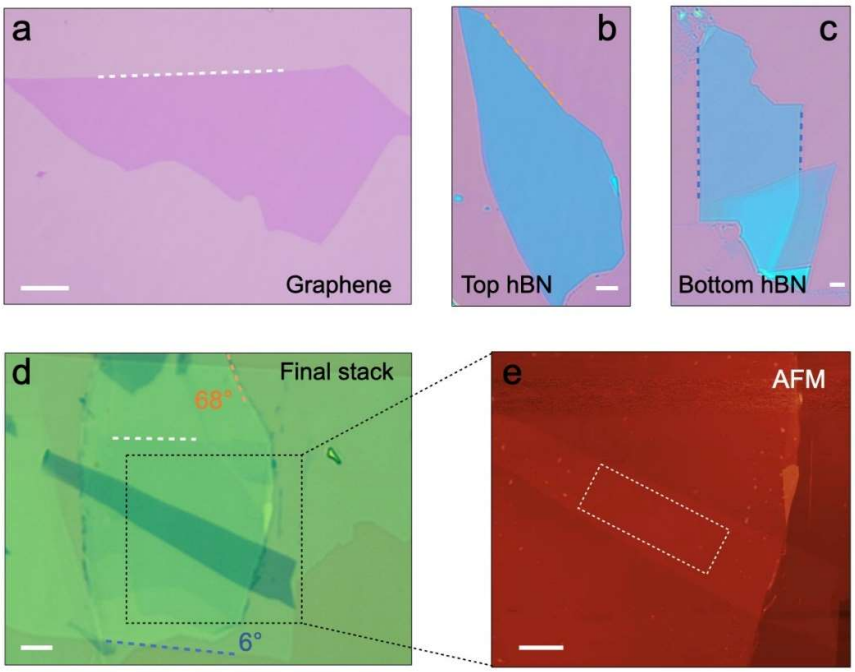

Extended Data Figure 1. | **Alignment to hBN. (a) - (c)** Optical micrographs of monolayer graphene (a), top (b) and bottom hBN (c) used for stacking the heterostructure shown in (d). **(d)** Optical image of the final stack. The numbers show relative misalignment angles between the white line (graphene edge) and bottom (blue) and top (orange) hBN edges. **(e)** Atomic force microscopy image of the stack shown in (d). The white dashed line box shows the device area. White bars correspond to 5 μm.

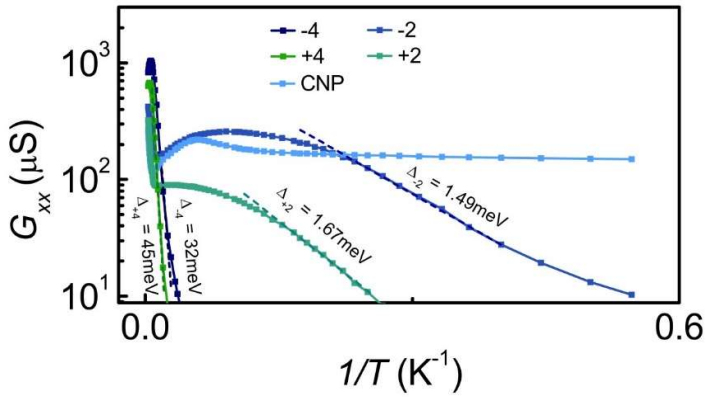

Extended Data Figure 2. | **Arrhenius plots for integer fillings ν=0,±2, ±4.** Extracted gaps are Δ_{-2}=1.49 meV, Δ_{+2}=1.67 meV, Δ_{-4}=32 meV and Δ_{+4}=45 meV. CNP resistance demonstrates a weak dependence on T suggesting no thermally activated gap thus pointing towards no explicit sublattice symmetry breaking due to alignment to hBN.

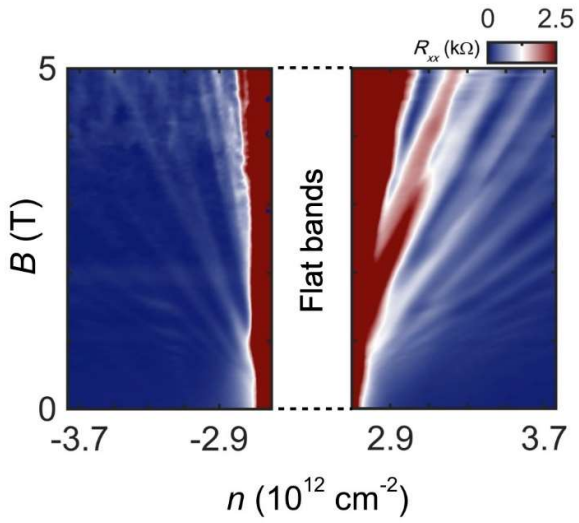

Extended Data Figure 3. | ***R**xx* **vs. *n* and *T* outside the flat band region.** The data demonstrates an absence of the satellite peaks that might be caused by a crystallographic alignment to hBN.

B. Extended data on AHE close to ν=+1 in MATBG.

In this section we show additional measurements of the AHE state close to ν=+1. We plot hysteresis loops taken at different charge carrier densities in Extended Data Fig. 4a for the same pair of contacts as in Fig. 1e in the main text (D-H in Extended Data Figure 7). In Extended Data Fig. 4b we show the evolution of anomalous Hall resistance $\Delta R_{yx}/2$ as a function of n and B extracted from a set of hysteresis loops close to ν=+1. Maximized AHE resistance ($\Delta R_{yx}/2$) densely localizes close to $\nu \approx$+0.84.

Extended Data Fig. 4c demonstrates $\Delta R_{yx}/2$ in units of h/e^2 as a function of n taken along the B=0 T line in Extended Data Fig. 4b. Upon increasing the superlattice filling from $\nu \approx$+0.84 to ν=+1 we observe a strong suppression of the AHE resistance, while the coercive field values keep increasing for both negative and positive B (blue and green data points in Extended Data Fig. 4b, respectively) indicative of a gradually suppressed coupling to the external field. In fact, we observe that the coercive field values maximize at $\nu \approx$+0.98 very close to the full integer filling. Upon closer inspection we find that this feature is likely associated with a weak magnetization reversal when the superlattice filling changes from the hole- to electron-doped side of ν =+1 similar to the previously reported pattern of quantized AHE at ν =+3 in hBN-aligned MATBG and twisted mono-bilayer graphene (see Extended Data Fig. 5).

We find this observation consistent with the divergence of the coercive field while the sample doping reaches exactly ν=+1. For a fixed valley polarization the total magnetization can change sign when passing through zero, therefore, being discontinuous when the chemical potential crosses the gap; the coupling to the magnetic field vanishes while approaching to ν=+1, thus, diverging the coercive field. In case of small Chern numbers (as in case of MATBG) the input of the bulk component of magnetization may be dominant resulting in a less robust magnetic states due to the higher influence of disorder. Ideally, in case of a minimized bulk magnetization, the edge magnetization would allow for the reversibility of the CCI at ν=+1. However, without alignment to hBN the probability to observe a fully reversible CCI is very low due to the absence of the exchange splitting between the Fermi level and the remote bands.

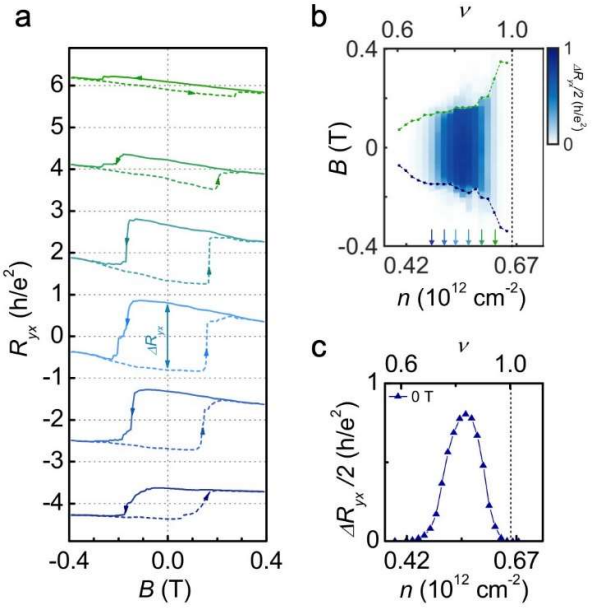

Extended Data Figure 4. | **Anomalous Hall effect at ν=+1 without alignment to hBN. (a)** A set of hysteresis loops taken at superlattice density fillings ν=0.74, 0.78, 0.82, 0.86, 0.90 and 0.94 (from bottom to top) and shifted by $2h/e^2$ for clarity. The data are obtained from the same pair of contacts as shown in Fig. 1e (D-H in Extended Data Figure 7). T=50 mK. **(b)** AHE resistance $\Delta R_{yx}/2$ as function of n and B. Green and blue dashed lines with symbols show coercive field values for positive and negative B, respectively. Colorscale is set to von Klitzing constant h/e^2. Arrow colors indicate hysteresis loops shown in (a). **(c)** Line trace taken along B=0 T shows maximized AHE resistance around ν=+0.84.

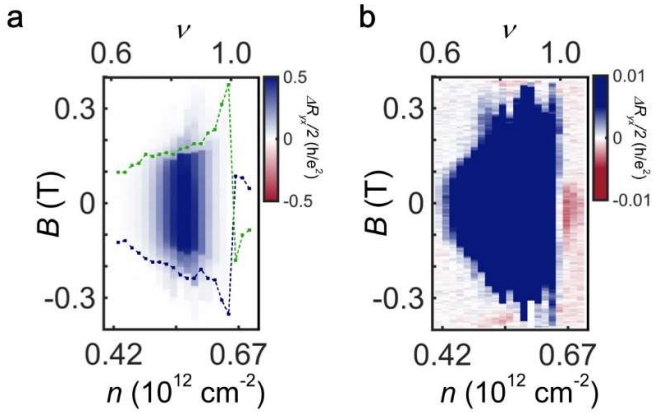

Extended Data Figure 5. | **Signatures of weak magnetization reversal at ν=+1. (a)** AHE resistance $\Delta R_{yx}/2$ as function of n and B taken from a pair of contacts C-I (see Extended Data Fig. 7), the same dataset reported in Fig. 4d on a different colorscale. **(b)** Same as (a) shown on a significantly enhanced colorscale reveals faint magnetization reversal signatures for charge carrier densities ν=+1+δ. Note an abrupt anomalous Hall resistance sign change from strongly negative to weakly positive upon crossing over ν=+1.

C. Correlated Chern insulators stabilized by magnetic field.

By applying higher magnetic field, we reveal a sequence of the quantum Hall-like plateaus that we assign to the high-field correlated Chern insulators. The line cuts shown in Extended Data Fig. 6 demonstrate the dominant sequence of the plateaus that match exceptionally well with the theory of the predicted CCIs at high magnetic fields above B_1 (Fig. 3 in the main text).

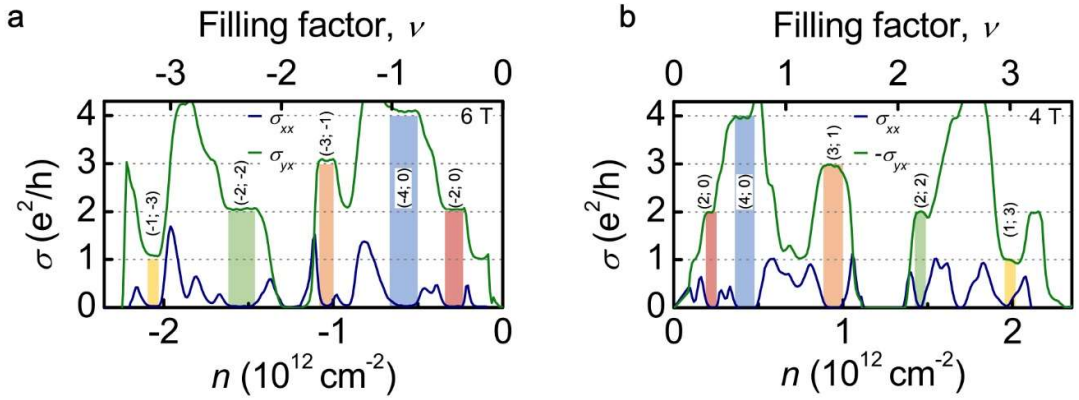

Extended Data Figure 6. | **Longitudinal and Hall conductance at high magnetic field.** Hall conductance σ_{yx} vs. n at **(a)** 6T and the valence flat band and **(b)** 4T and the conductance flat band. The sequence reveals a set of strongly quantized σ_{yx} with (C, ν) = (±2, 0), (±4, 0), (±3, ±1), (±2, ±2) and (±1, ±3).

D. Angle homogeneity in the studied sample.

We perform two terminal conductance measurements between pairs of adjacent contacts to mesoscopically probe twist angle homogeneity. All pairs exhibit a presence of strong correlations visible by the emergence of CI conductivity minima at ν=+1, ±2, +3. This indicates a very low twist angle disorder, which can also mediate the observation of AHE state at ν=+1.

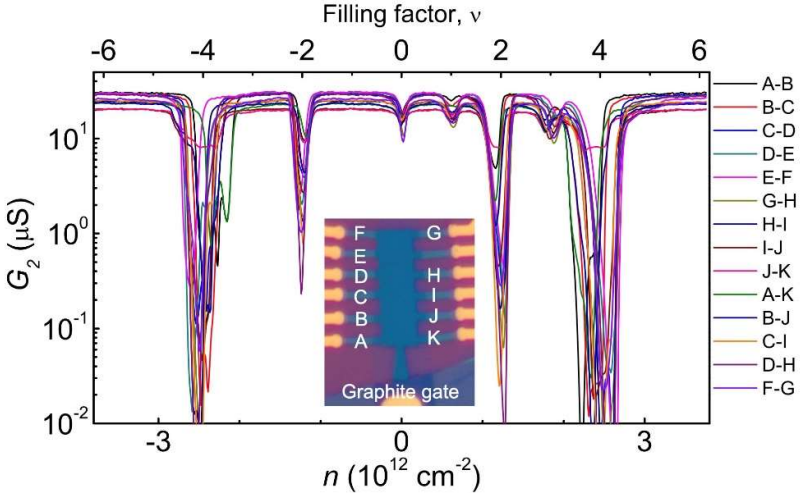

Extended Data Figure 7. | **Two-terminal conductance data.** Line traces correspond to the two terminal conductance G_2 vs. n taken for all available pairs of contacts. The legend indicates corresponding pairs.

We quantify the twist angle disorder by extracting twist angles relative to the pair of contacts reported in the main text (C-D in Extended Data Figure 7). First, we find the deviation of the charge carrier density corresponding to the $\nu = \pm 2$ for all pair of contacts. Second, we compare this value to the one extracted from the SdH oscillations for the pair C-D (see Methods). Last, we extract a conformed twist angle using the formula $n_s = 8\theta^2/\sqrt{3}a^2$. As a result, we find the deviations of the charge carrier density corresponding to the fully filled superlattice, which fall in the range $n_s = (2.71\pm0.04)\times10^{12}$ cm^{-2}. Thus, the absolute twist angle variation across the sample is $\theta = 1.08\pm0.01°$.

E. Hall density data.

We extract the Hall density from the low-field Hall resistance data using the relation $n_H = -B/eR_{xy}^{antisym}$, where $R_{xy}^{antisym} = (R_{xy}(B) - R_{xy}(-B))/2$ is an antisymmetric component of the measured Hall resistance used to eliminate any symmetric-in-B input. The Hall density experiences a few clear resets along the charge carrier line indicative of new Fermi surface formations at $\nu = +1, \pm2, \pm3$. This data is consistent with high magnetic field data shown in Fig. 2 in the main text, where we observe new sets of well-quantized QH-like plateaus emanating from each of these integer fillings. Note the switch of Hall density sign inside the AHE region denoted by the black dashed lines.

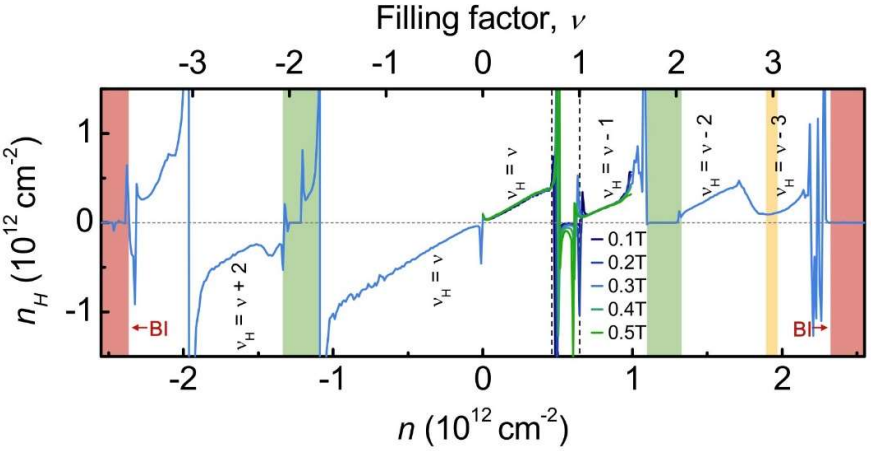

Extended Data Figure 8. | **Hall density measurements.** The light-blue line trace shows n_H vs. n taken at 0.3 T. The light green and light yellow stripes show the position of CI states, at which we also observe clear signatures of Hall density resets. Black dashed lines mark the region, where we observe signatures of AHE. Interestingly, the Hall density changes sign inside and outside this region. In addition, we plot Hall density n_H vs. n close to $\nu = +1$ for other magnetic field values (0.1, 0.2, 0.4, 0.5 T).

F. Additional data on superconductivity and magnetic hysteresis.

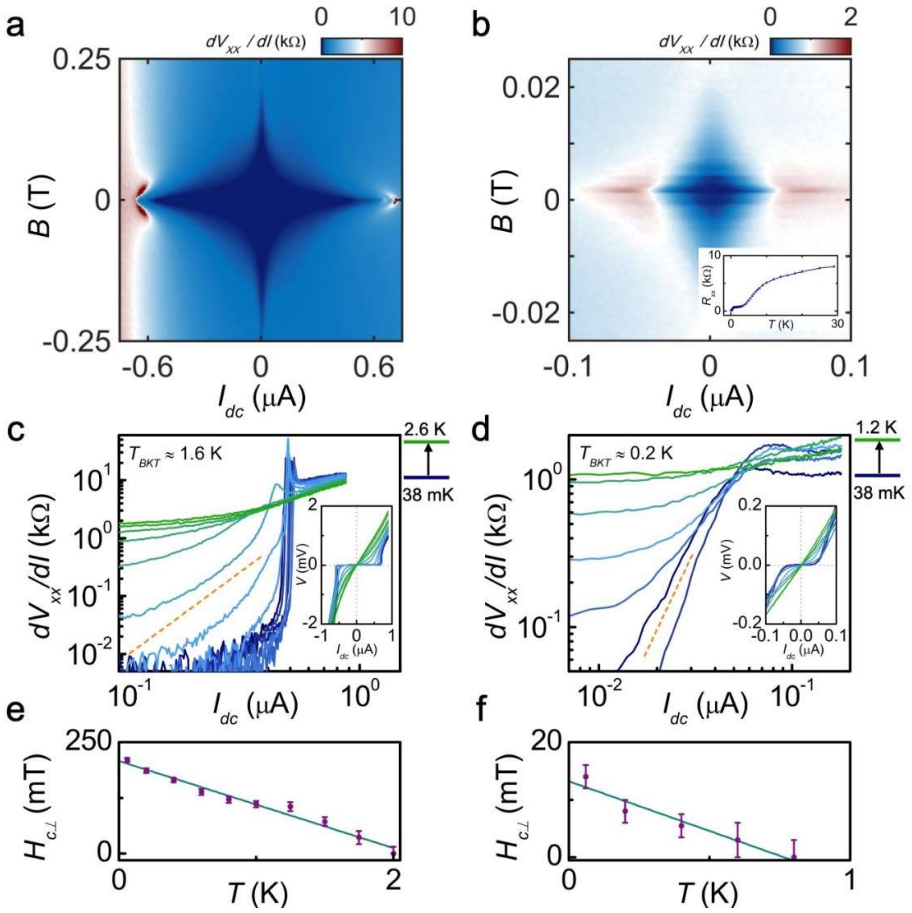

Extended Data Figure 9. | **Full characterization of SC phases.** The left- (right-) hand side of the figure corresponds to SC pockets with optimal doping ν=-2.16 (ν=2.10). **(a)-(b)** Differential resistance dV_{xx}/dI as a function of direct current bias I_{dc} and B. AC excitation current used for this measurement is I_{ac} = 2 nA. Fraunhofer-like oscillation patterns are clearly visible in (b). The inset in (b) shows R_{xx} vs. T for SC at optimal doping ν=2.10. **(c)-(d)** Berezinskii–Kosterlitz–Thouless (BKT) measurements of differential resistance dV_{xx}/dI versus I_{dc} taken at different temperatures. BKT transition temperature T_{BKT} is defined by fitting to $dV_{xx}/dI \propto I^2$. The insets show I-V curves that show critical current of approximately 0.69 μA (ν=-2.16) and 0.06 μA (ν=2.10). **(e)-(f)** Ginzburg-Landau coherence length measurements. Critical field $H_{c\perp}$ versus T taken at half of normal state resistance values. The cyan lines are the best linear fit to data. We extract ξ_{GL} = 38 nm (e) and ξ_{GL} = 153 nm (f) from $H_c=(\Phi_0/(2\pi\xi_{GL}^2))(1-T/T_{c0})$, where $\Phi_0=h/2e$ is superconducting flux quantum and T_{c0} is the mean-field temperature at zero B.

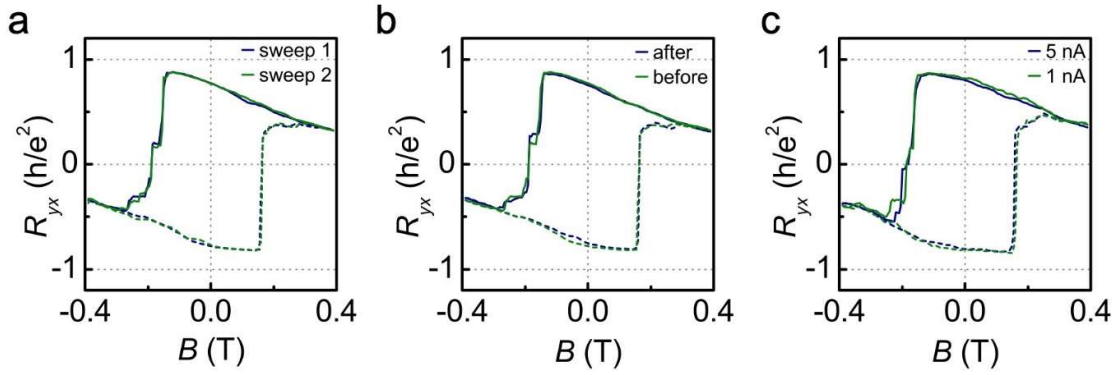

Extended Data Figure 10. | **Repeatability of hysteresis loops. (a)** $R_{yx}(B)$ line traces for two different sweeps taken at ν=+0.84. The sweeps are taken 48 hours apart at 50 mK. **(b)** $R_{yx}(B)$ line traces taken before and after thermocycling the sample from 50 mK to 5 K and back to 50 mK at ν=+0.84. **(c)** $R_{yx}(B)$ line traces taken for AC excitation currents 1 nA and 5 nA at ν=+0.82. The dashed (solid) lines corresponds to ascending (descending) B-field.

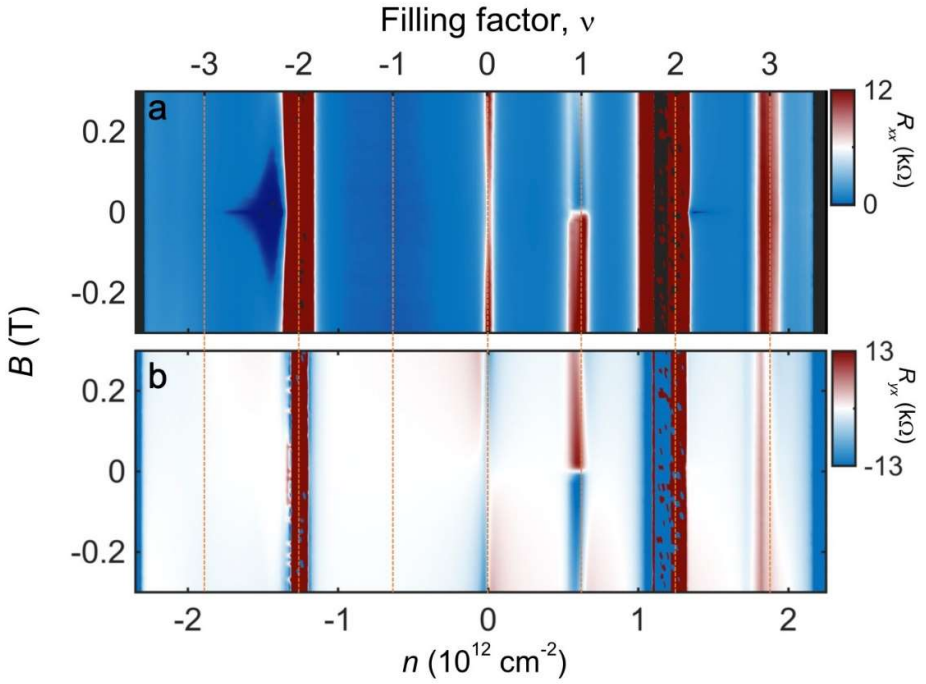

Extended Data Figure 11. | **High resolution scan for the low range of *B*-field. (a)** R_{xx} and **(b)** R_{yx} as a function of n and B for low range of the magnetic fields taken at 50 mK. Note an abrupt switch of sign of R_{yx} at $\nu\approx$+1 upon crossing B=0 T line. Dark grey regions in (a) indicate quenched drain current due to the high sample resistance thus leading to unreliable voltage readings.

G. Competition of correlated Chern insulator states under magnetic field at ν=+1.

At integer fillings of the moiré flat bands, theoretical works have predicted a series of trivial and topological insulating states that are very close in energy. The ground state phase diagram seen by experiments vary from sample to sample which suggests that the exact energetic order of these states is sensitive to experimental parameters. When a magnetic field is applied, the total energies of these states as well as their relative order will be altered. Here we focus on the correlated insulating states at ν=+1.

We perform self-consistent Hartree-Fock mean-field calculations to study the ground states at integer filling factors. Details of the calculation can be found in SI Ref[1] with an additional assumption that the remote band degrees of freedom are frozen, an approximation justified by the fact that the flat bands are relatively isolated from the remote bands. Here we used typical bandstructure parameters θ=1.1° and T_{AA}/T_{AB}=0.6, and, as an example, an interaction strength parameter ϵ^{-1}=0.03 which can easily change as the distance to the nearby metallic gate is varied (see SI Ref[2]).

At ν=+1, we found that the lowest energy states are insulating and spontaneously break C_2T symmetry and the approximate U(4) flavor symmetry. As a result of flavor symmetry breaking, these states are both spin and valley polarized with one fully filled flavor, which is chosen spontaneously, and three half-filled flavors. The half-filled flavors have a gap between valence and conduction bands due to C_2T symmetry breaking and a nonzero Chern number which, within the flat band Hilbert space, can be either +1 or -1. States with total Chern number C=±1 and ±3 are thus possible with the former being slightly lower in energy as shown by Ref[3]. As discussed in the main text, at zero or low magnetic field one expects that C=±1 states are more likely to be the ground state. The quasiparticle bands of the fully-filled flavor remains gapless with band touching at Dirac points. An overall energy gap is formed (orange region in Extended Data Figure 12) whose size depends on the strength of the Coulomb interaction. Several studies have also found ground states to be inter-valley coherent which we will discuss in later part of this section. In either case, the physics of the problem remains similar, as the charged ±1 excitation dispersions (Hartree-Fock bands) do not depend on the details of the polarization of the ground state (Ref.[4]).

The change in total energy due to applied magnetic field **B** can be described by the magnetic potential energy ΔE=**-B**·**M**, where **M** is the total magnetization, which includes both spin and orbital contributions. For orbital Chern insulators (see Ref[5]) considered here, they only differ in orbital magnetization so we can ignore the spin magnetization. We calculate the orbital magnetization approximately by treating the mean-field quasiparticle states as non-interacting Bloch electrons.

Extended Data Figure 12 shows the orbital magnetization of the C=-1 state which has one fully-filled flavor and three half-filled flavors. For the fully-filled flavor, Chern numbers of its conduction and valence bands cancel each other; because the fully-filled density matrix cannot have C_2T breaking order within the flat-band Hilbert space, its magnetization vanishes. For half-filled flavors, the Chern numbers can be either +1 or -1 depending on their spontaneous sublattice polarization. Inside the gap, orbital magnetization is linearly proportional to the Chern number (e.g. Ref[5]) and its slope has the same sign as the Chern number.

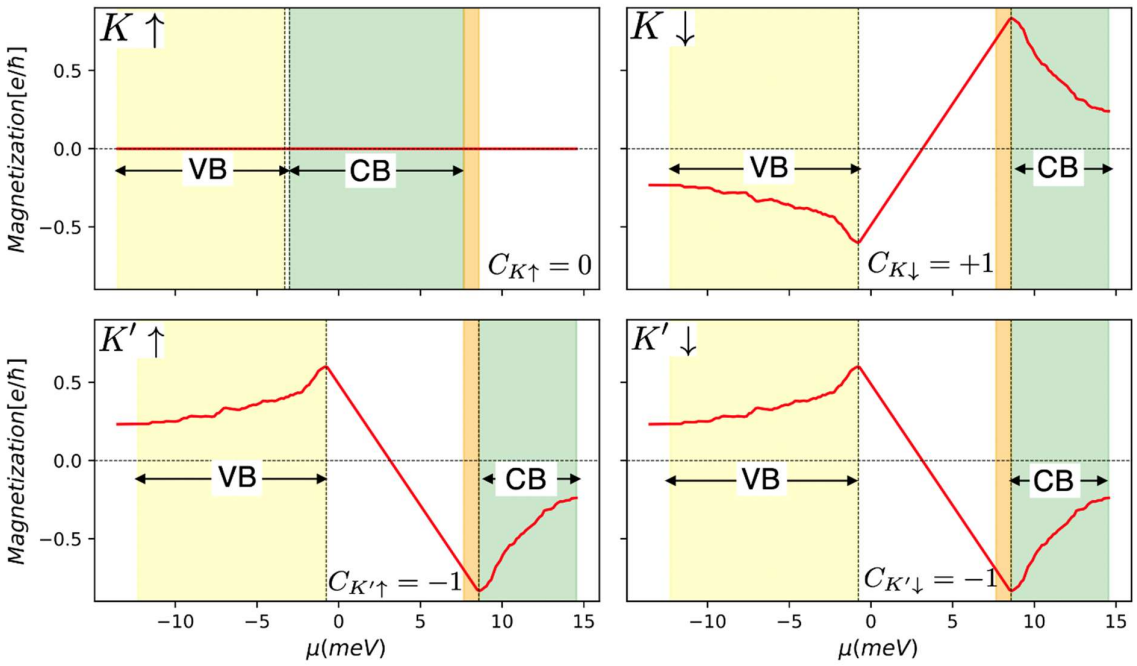

Extended Data Figure 12. | **Magnetization of the (C, ν) = (-1, +1) mean-field insulating state as a function of chemical potential μ.** The insulating state has one flavor fully filled flavor $K\uparrow$, which remain gapless, and three half-filled flavors $K\downarrow, K'\uparrow$, and $K'\downarrow$, all of which have an interaction induced gap. The yellow and light green regions mark the energy span of the quasiparticle valence band (VB) and conduction band (CB), respectively. The orange region marks the overall energy gap, once kinetic energy has been introduced (the non-flat-band case, where the kinetic energy in the BM model is also taken into account, along with the strong Coulomb interaction).

The total orbital magnetization **M** is a sum of the contributions from the four flavors. The sign of **M** inside the gap is in general not definite because the (overall) gap is very likely to span a larger energy range which includes the point at which **M** changes sign. For instance, at stronger interaction, the fully-filled flavor is lowered more in energy due to enhanced exchange splitting such that the overall gap is increased. If we consider the slightly doped cases on the hole or electron sides of ν=+1, **M** has a definite sign. Because **M** normally changes sign across the gap, one expects the hysteresis loop in the Hall resistance also flips sign when going from hole doping side (ν<+1) to electron doping side (ν>+1). This property also agrees with the experimental observations in Figure 4d and 4e. The magnitude of the magnetization is not exactly the same on the two sides of the gap. When the non-local tunneling effect is included (see discussions in the next section), the magnitude of the magnetization is much smaller on the ν>+1 side. The fact that the hysteresis loop changes sign at ν=+1 suggests that C=+1 state is seen on ν>+1side, but only weakly developed. This agrees with the nonlocal tunneling effect that magnetization is small on the ν>+1 side, so it is hard for magnetic field to coarsen domain configurations.

At higher enough magnetic field, the magnetization energy eventually wins over the zero-field total energy difference and favors state with larger magnitude of magnetization. The states with |C|=3 have similar quasiparticle dispersions as the |C|=1 states, however, because magnetization of the half-filled flavors have the same sign, they have larger magnitude of magnetization. Indeed the C=+3 Chern insulator state is seen here at higher field B>1 T and

ν>+1+δ (δ>0) with a well-quantized Hall conductance as shown in Figure 4c. We also expect C=-3 in the hole doped side ν<+1-δ, however, it is not seen here possibly because at the filling factor range ν<+1-δ, the ground state remains flavor symmetry unbroken leading to four-fold degenerate Landau levels as is indeed seen in this range. Exactly at which filling factor the flavor symmetry breaking order emerges depends primarily on the location of the van Hove singularity as discussed in Ref[6].

In above mean-field calculations, we have not allowed inter-valley coherence. Several theoretical works, including the work (Ref[3]) by one of the authors, have predicted that states with valley pseudo-spin component in the in-plane direction have lower energy than the spin-valley polarized states. However, because valley coherence mixes bands with the same Chern number, and the fact that the predicted valley anisotropy is rather weak, we expect the change in quasiparticle characters comparing to the spin-valley polarized states is only qualitative and small. This is in agreement with Ref[4] where, in the flat-band limit, the same excitation spectrum is found above any of the ground state, be they valley coherent or valley polarized. As a numerical test, we performed self-consistent mean-field calculations allowing inter-valley channels. The resulting dispersions are showing in Extended Data Figure 13. We find that the inter-valley coherent (IVC) state is slightly lower in energy. Comparing the dispersion of the IVC state with that of the polarized state, we see that its dispersion only changes slightly with a small splitting in the region where bands from the two valleys are degenerate in the spin-valley polarized state. We thus expect that the physics presented above using the spin-valley polarized states holds in IVC state case.

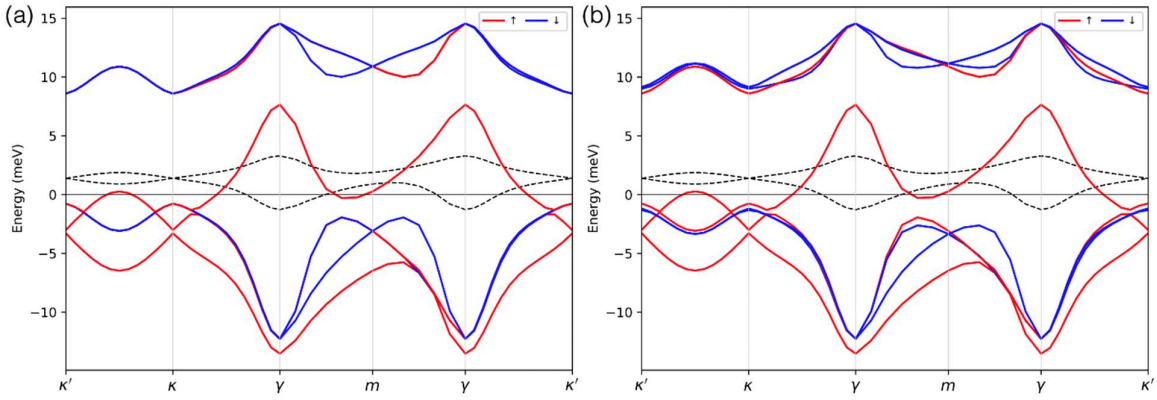

Extended Data Figure 13. | **Quasiparticle dispersion of (a) the spin-valley polarized state and (b) the inter-valley coherent state.** The red (blue) solid lines corresponds to spin up (down) bands. The spin up flavor has one more band filled than the spin down flavor. We note that along certain high symmetry lines the dispersions overlap. The dashed lines represent non-interacting bands.

A heuristic way of understanding the stabilization of the C=-1 state at low magnetic field (although during hysteresis, both C=+1 and C=-1 are observed and explained by our magnetization argument) is through their Landau level spectrum Extended Data Fig. 14a. Assume at zero magnetic field there exists two degenerate ground states, one with C=+1 and one with C=-1. These two ground-states have identical excitation spectrum. In field, they however differ by one zero mode, which, at constant filling ν=+1, pins the Fermi level to be at the top/bottom of the valence/conduction band for Chern number +1/-1. By counting the energies of the occupied LL below the Fermi level, the C=-1 is favored in low B. The property

that positive magnetic fields tend to favor C=-1 states for ν<+1 and C=+1 states for ν>+1 can be understood by the following heuristic argument. The total energy vs. filling factor curve has a cusp at the densities of the gaps illustrated in Extended Data Fig. 14b. For positive fields the C=+1 cusp occurs at a higher density than the C=-1 gap, leading to the illustrated energetic ordering illustrated vs. band filling.

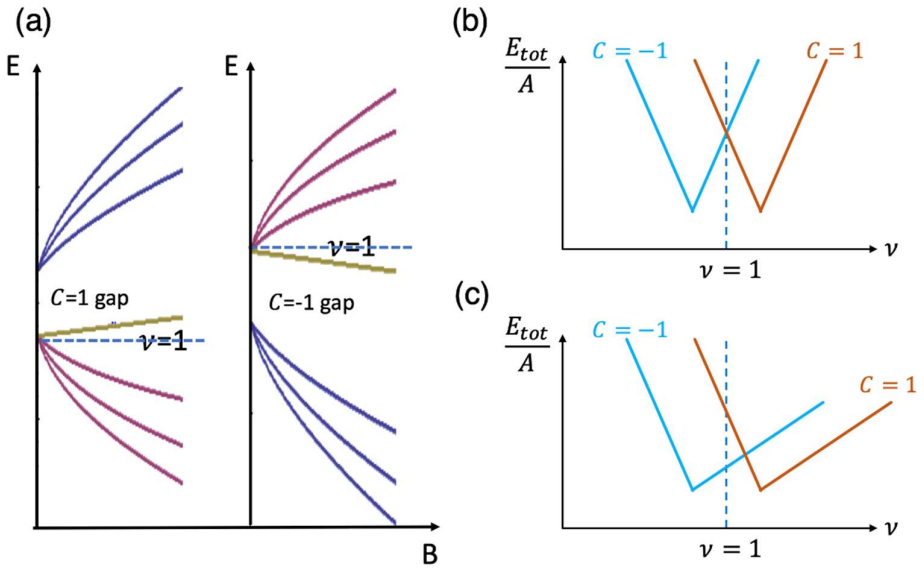

Extended Data Figure 14. | **(a)** Landau level spectrum of C=+1 and C=-1 Chern insulators with identical dispersion. The difference rests in the "zero-mode" Landau Level which has opposite in-field behavior for the two cases. **(b)** Total energy per area for states with C=+1 and C=-1 in the gap under finite positive magnetic field B>0. The cusps are where the $|C|$=1 gaps are located. **(c)** Same plot as in (b) for states with smaller magnetization on the electron doped side due to nonlocal tunneling effect discussed in next section.

H. Effect of particle-hole asymmetry

The original Bistritzer-MacDonald (BM) continuum model has an approximate particle-hole symmetry based on which one would expect a particle-hole symmetric phase diagram with respect to ν=0. Instead almost all the experiments have shown certain degree of particle-hole asymmetry in MATBG phase diagram. One possible origin, which is not due to extrinsic factors, is the nonlocal tunneling that is ignored in the BM model (see Ref[6] and references therein). Here we examine the effect of this nonlocal tunneling on the orbital magnetization.

To show the effect of the particle-hole asymmetry, we plot the orbital magnetization of non-interacting bands from a nonlocal continuum model. ω_{NL} characterizes the strength of the nonlocal tunneling which in turn determines the degree of particle-hole asymmetry. As ω_{NL} increases, the magnetization increases uniformly inside the gap and the point of zero magnetization shifts to the right side of the gap. The Chern bands used here all have C=-1 inside the gap. For bands with C=+1, the magnetization curve flips sign and decreases uniformly within the gap as ω_{NL} increases. For both cases, the point of zero magnetization shifts away from the middle of the gap towards the bottom of the conduction band. As discussed in the previous section, this effect causes the magnitude of the magnetization smaller on the high-filling factor side of the gap – in agreement with our experimental observations.

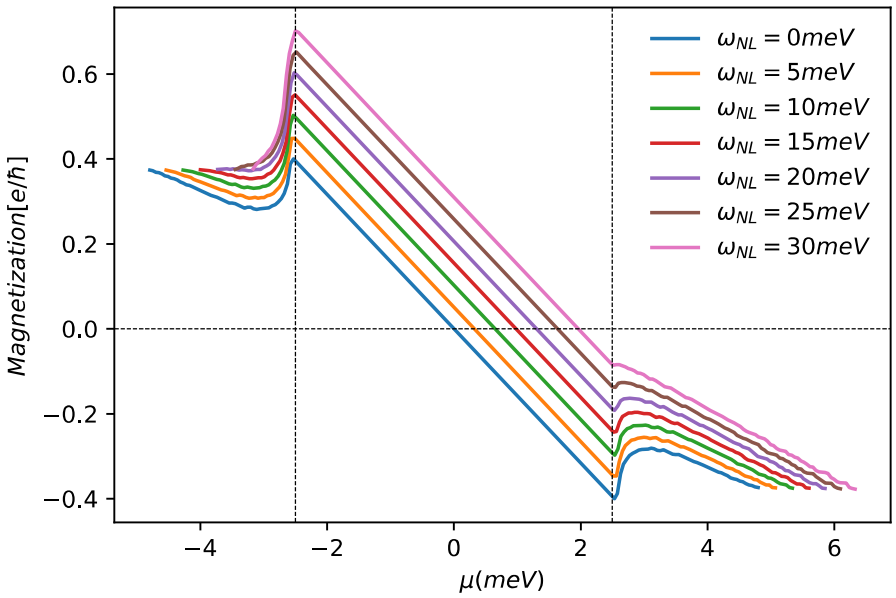

Extended Data Figure 15. | **Magnetization of particle-hole asymmetric flat bands.** The degree of the asymmetry is determined by the strength of the nonlocal tunneling ω_{NL}. A C_2T breaking potential is added manually which is necessary to generate finite orbital magnetization. The dashed lines on the left roughly marks the top of the valence band while that on the right roughly marks the bottom of the conduction band. We have shifted the energy axis, so the center of the gap for different ω_{NL} sit at same energy for the purpose of comparison.

Supplementary References

1. Xie, M. & MacDonald, A. H. Nature of the Correlated Insulator States in Twisted Bilayer Graphene. *Phys. Rev. Lett.* **124**, 97601 (2020).
2. Stepanov, P. *et al.* Untying the insulating and superconducting orders in magic-angle graphene. *Nature* **583**, 375–378 (2020).
3. Lian, B. *et al.* TBG IV: Exact Insulator Ground States and Phase Diagram of Twisted Bilayer Graphene. *arXiv Prepr. arXiv2009.13530* (2020).
4. Bernevig, B. A. *et al.* TBG V: Exact Analytic Many-Body Excitations In Twisted Bilayer Graphene Coulomb Hamiltonians: Charge Gap, Goldstone Modes and Absence of Cooper Pairing. *arXiv Prepr. arXiv2009.14200* (2020).
5. Zhu, J., Su, J.-J. & MacDonald, A. H. Voltage-Controlled Magnetic Reversal in Orbital Chern Insulators. *Phys. Rev. Lett.* **125**, 227702 (2020).
6. Xie, M. & MacDonald, A. H. Weak-field Hall resistivity and spin/valley flavor symmetry breaking in MAtBG. *arXiv Prepr. arXiv2010.07928* (2020).